ACS Energy LETTERS

http://pubs.acs.org/journal/aelccp

# Hybrid Thermally Activated Nanocluster Fluorophores for X-ray Scintillators

Peng Yuan,[+] Tengyue He,[+] Yang Zhou,[+] Jun Yin,[+] Hansong Zhang, Yongcao Zhang, Xiting Yuan, Chunwei Dong, Renwu Huang, Wenyi Shao, Shulin Chen, Xin Song, Renqian Zhou, Nanfeng Zheng, Mutalifu Abulikemu, Mohamed Eddaoudi, Mehmet Bayindir,* Omar F. Mohammed,* and Osman M. Bakr*

Cite This: *ACS Energy Lett.* 2023, 8, 5088−5097

Read Online

ACCESS | Metrics & More | Article Recommendations | Supporting Information

**ABSTRACT:** **Thermally activated delayed fluorescence (TADF) X-ray scintillators have attracted increasing attention because of their theoretical ability to utilize 100% radiation-induced excitons. However, their scintillation performance is severely hampered by their typically low X-ray attenuation efficiencies or mechanochromic properties. Here, we demonstrate hybrid organic−inorganic TADF scintillators with remarkably high X-ray absorption cross sections based on non-mechanochromic $Cu_2X_2$ (X = Cl, Br, or I) nanoclusters. The $Cu_2X_2$ nanoclusters display radioluminescence light yields as high as 175 000 photons $MeV^{-1}$, attributable to their low self-absorption and spatially separated HOMO and LUMO orbitals. Furthermore, because of their non-mechanochromic properties, these nanoclusters can be formed into scintillating screens with excellent radiation and humidity stability via soft-pressing. The fabricated TADF scintillating screens display a high X-ray imaging efficiency, benefiting from their high light yields and high spatial resolutions (∼30 lp $mm^{-1}$). This work highlights the promise TADF $Cu_2X_2$ nanocluster-based scintillators have in meeting the demanding requirements of cutting-edge X-ray imaging.**

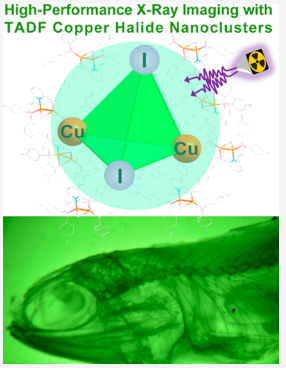


X-ray scintillation plays an indispensable role in medical diagnosis, industrial inspection, and security, given its ability to convert high-energy ionizing radiation into readily detectable low-energy visible photons.[1−5] New scintillators with enhanced abilities for converting X-rays to visible light are actively being explored to improve radioluminescence (RL) intensity and imaging quality.[6−14] One promising avenue of investigation is the use of thermally activated delayed fluorescence (TADF) materials,[9−14] particularly the hybrid organic−inorganic TADF-like Cu(I) complexes. Theoretically, these TADF-like Cu(I) complexes can achieve up to 100% internal quantum efficiency through the reverse intersystem crossing (RISC) process. This process facilitates the transition of their excitons from the lowest triplet excited state ($T_1$) to the lowest singlet excited state ($S_1$),[15−17] thereby significantly enhancing the efficient utilization of radiation-induced triplet excitons.

Compared to organic TADF scintillators, TADF-like Cu(I) complexes are ideal systems for high-performance scintillators, as they contain heavy atoms and display appreciable RL properties under ambient conditions.[9,11−13] The structural tunability of Cu(I) complexes allows for one to obtain a small energy gap ($\Delta E_{ST}$) between $S_1$ and $T_1$, as well as strong spin−orbit coupling (SOC).[18−21] The combination of these properties opens up new possibilities for radiation detection and imaging,[12,13] as it can overcome the trade-off between high quantum yield (QY) and small $\Delta E_{ST}$ values that organic TADF systems have.[22−24]

These advantages have spurred the development of scintillators in the family of hybrid organic−inorganic TADF Cu(I) halide complexes, such as $Cu_4I_4$,[11,25] $Cu_3Br_3$,[26] and $Cu_1I_1$,[9] which have shown promising light yields (∼12 842, ∼20 000, and ∼30 000 photons $MeV^{-1}$, respectively) and low detection limits. The radioluminescence properties of these materials are attributed to the combination of their heavy $[CuI/Br]_n$ core and high photoluminescence efficiency.[9,11,25,26] While previous studies have confirmed the potential of Cu−I nanoclusters for scintillator applications,[2,7,27,28] the light yields of such nanoclusters still require significant improvement in order to be on par with state-of-the-art imaging scintillators.[7,8,10,29] Moreover, their stability and mechanochromism[30,31] are likely to hinder their processing into high-quality scintillator screens via low-cost mechanical methods.[32−34]

**Received:** September 27, 2023
**Revised:** November 3, 2023
**Accepted:** November 6, 2023






https://doi.org/10.1021/acsenergylett.3c02050
*ACS Energy Lett.* 2023, 8, 5088−5097

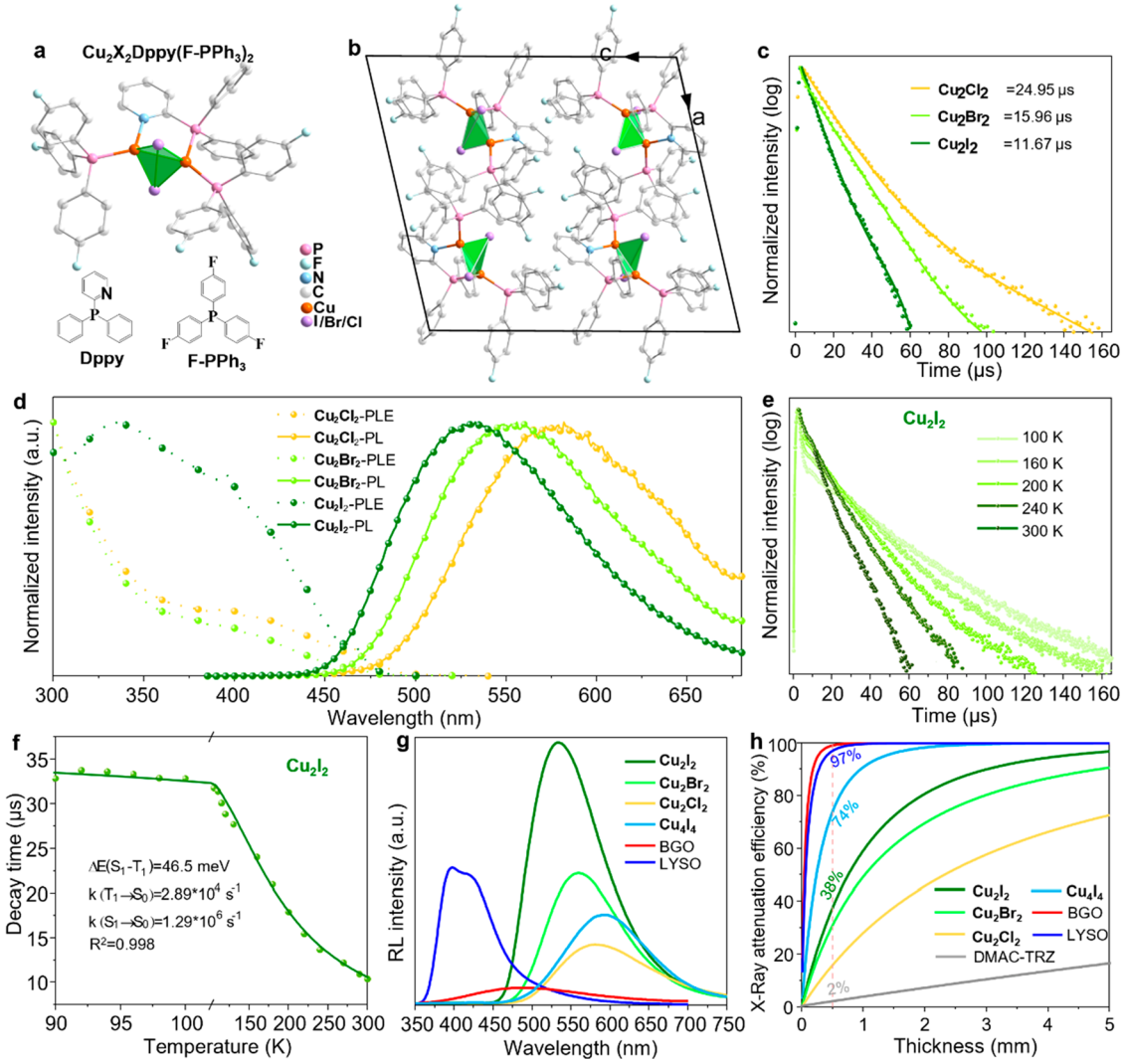


**Figure 1. Characterization of the $Cu_2X_2$ crystals. (a) Molecular structures and (b) packing mode of the $Cu_2X_2$ crystals. (c) Excited-state lifetimes upon excitation at 365 nm. (d) Normalized emission and excitation spectra. (e) Temperature dependence of the excited-state lifetimes in the range of 100−300 K for $Cu_2I_2$. (f) Plot of emission decay lifetime against temperature (90−300 K) for $Cu_2I_2$; the green line represents the fit according to the TADF equation. (g) RL spectra of the $Cu_2X_2$ crystals compared with reference scintillators, namely, BGO, LYSO, and the $Cu_4I_4$ nanocluster (50 kV and 50 μA). (h) Calculated X-ray attenuation efficiencies of $Cu_2X_2$, $Cu_4I_4$, DMAC-TRZ, BGO, and LYSO versus their thicknesses across the entire range of X-ray photon energies (0−50 keV) (Figure S9).**

In this study, we report a series of hybrid organic−inorganic non-mechanochromic TADF **$Cu_2X_2$** nanoclusters for X-ray scintillation and imaging with the highest light yield in their class. The TADF Cu(I) halide nanoclusters $[Cu_2I_2(Dppy)(F\text{-}PPh_3)_2]$,[35] $[Cu_2Br_2(Dppy)(F\text{-}PPh_3)_2]$, and $[Cu_2Cl_2(Dppy)(F\text{-}PPh_3)_2]$, hereafter abbreviated as **$Cu_2X_2$**, consisting of diphenyl-2-pyridylphosphine (Dppy), tri-(4-fluorophenyl)-phosphine) (F-$PPh_3$), and halogen atoms (I, Br, or Cl), exhibit strong photoluminescence, X-ray stopping power, and $[Cu_2X_2]$-to-ligand charge transfer characteristics. Consequently, these TADF nanoclusters display a record scintillation performance, having a relative light yield of up to 175 000 photons $MeV^{-1}$. We undertook a series of characterizations, including theoretical modeling, to elucidate the underlying mechanisms for the pronounced radioluminescence properties observed in the **$Cu_2X_2$** nanoclusters, especially in **$Cu_2I_2$**. Furthermore, we demonstrate that flexible **$Cu_2X_2$** scintillation films can be fabricated by using a soft-pressing strategy. This method not only improves the quality of the scintillator but also augments its imaging capabilities by enhancing the crystallographic alignment of the **$Cu_2X_2$** microcrystals and reducing the optical scattering in the scintillator screens. We showcase the potential applications of these flexible scintillator films in X-ray imaging, achieving a high spatial resolution (∼30 lp (line pairs) $mm^{-1}$) with a high resistance to humidity and radiation.

Single crystals of $Cu_2X_2(Dppy)(F\text{-}PPh_3)_2$ (X = Cl, Br, or I) were obtained by the layering method with dichloromethane (DCM) and *n*-pentane.[35,36] Notably, neither the structures of the bromide nor the chloride of this class of **$Cu_2X_2$** nanoclusters have been previously characterized structurally. As determined by single-crystal X-ray diffraction, the **$Cu_2X_2$** nanoclusters are isostructural and crystallize into the space group of $P2_1/c$ (Table S7).[35] They have similar cell parameters and butterfly shaped $[Cu_2X_2]$ cores, which are indicative of a tetrahedral coordination geometry (Figure 1a,b and Table S7). The distance between the two copper atoms is approximately 2.70 Å in all of the obtained structures (Figure S1). The main



https://doi.org/10.1021/acsenergylett.3c02050
ACS Energy Lett. 2023, 8, 5088−5097

bond lengths and angles (X−Cu−X, P−Cu−P, and N−Cu−P) of the $\mathbf{Cu_2X_2}$ nanoclusters are listed in Table S1.

The steady-state photoluminescence (PL) spectra of these $\mathbf{Cu_2X_2}$ nanoclusters show broad emission bands in the visible range, centered approximately at 533 (I), 553 (Br), and 580 (Cl) nm, respectively (Figure 1d). Interestingly, a clear trend of the emission maxima is observed that is dependent on the halides, as a blue-shift occurs from $\mathbf{Cu_2Cl_2}$ to $\mathbf{Cu_2I_2}$.[36] As shown in Figure 1c, the PL decay times at room temperature (rt) also demonstrate the same trend, gradually decreasing from 24.95 $\mu$s for $\mathbf{Cu_2Cl_2}$ to 11.67 $\mu$s for $\mathbf{Cu_2I_2}$. We further investigated the PL characteristics of $\mathbf{Cu_2X_2}$ by examining their temperature dependence in the range of 90−300 K. The emission energy increased as the temperature increased from 90 to 300 K, resulting in a 23, 17, and 7 nm blue-shift of the maximum emission under an excitation at 365 nm for $\mathbf{Cu_2Cl_2}$, $\mathbf{Cu_2Br_2}$, and $\mathbf{Cu_2I_2}$, respectively (Figures S2, S3, and S5). This blue-shift is a result of the thermal activation of the energetically higher-lying $S_1$ state above $T$ = 90 K. Furthermore, this temperature-dependent enhancement in luminescence demonstrates an excellent characteristic of reverse intersystem crossing (RISC) during triplet-to-singlet up-conversion.[37,38]

To investigate the potential TADF properties of these nanoclusters, we also measured the temperature-dependent emission decay times, which varied gradually from 90 to 300 K (Figures 1e, S2, S4, and S6). As the temperature increased, the fast RISC process to the $S_1$ state occurred, which initiated an additional radiative TADF process via the decay path from the $S_1$ state. This resulted in a noticeable blue-shift in the emission spectrum and a significant reduction in the emission decay time, as the emitting $S_1$ state lies higher in energy than the $T_1$ state. The modified Boltzmann equation was used to fit the emission decay lifetimes $\tau$ (for $T$ = 90 to 300 K), which yielded an activation energy of $\Delta E(S_1-T_1)$ = 117 ($\mathbf{Cu_2Cl_2}$), 100 ($\mathbf{Cu_2Br_2}$), and 46.5 meV ($\mathbf{Cu_2I_2}$), respectively (Figures 1f, S4a, and S6a). Additionally, the radiative rates $k(S_1-S_0)$ and $k(T_1-S_0)$ that were observed for $\mathbf{Cu_2I_2}$ were $1.29 \times 10^6$ and $2.89 \times 10^4$ $s^{-1}$, respectively, corresponding to a prompt fluorescence decay time of $\tau(S_1-S_0)$ = 775 ns and a phosphorescence decay time of $\tau(T_1-S_0)$ = 34.6 $\mu$s. In comparison, $\mathbf{Cu_2Br_2}$ and $\mathbf{Cu_2Cl_2}$ show slightly higher $k(S_1-S_0)$ and lower $k(T_1-S_0)$ values than $\mathbf{Cu_2I_2}$ (Table S2). The radiative decay rate ($k_r$) can be determined using emission QYs and decay times, and it was found to be $2.18 \times 10^4$ ($\mathbf{Cu_2Cl_2}$), $5.96 \times 10^4$ ($\mathbf{Cu_2Br_2}$), and $7.78 \times 10^4$ $s^{-1}$ ($\mathbf{Cu_2I_2}$) at 300 K, respectively. At rt, the fitted curve displays a downward trend rather than a plateau, indicating that rt emission includes contributions from delayed fluorescence and phosphorescence, corresponding to triplet-state emission at low temperatures and singlet-excited-state emission at high temperatures.[15,16,39] Additionally, the ratio $I(S_1)/I(T_1)$ at ambient temperature is approximately 2.20 ($\mathbf{Cu_2Cl_2}$), 3.30 ($\mathbf{Cu_2Br_2}$) and 2.50 ($\mathbf{Cu_2I_2}$), respectively, indicating that TADF is the predominant factor in the emission spectra (Table S3).[18] The alignment between the activation energy and the spectral shift with an increase in temperature supports the assignment of ambient temperature emission as TADF. By combining the TADF and phosphorescence pathways, the decay times of the $\mathbf{Cu_2X_2}$ nanoclusters are significantly reduced compared to phosphorescent Cu(I) complexes, which typically exhibit decay times that are of the order of several hundred microseconds, even up to milliseconds.[40] In particular, $\mathbf{Cu_2I_2}$ shows a smaller $\Delta E(S_1-T_1)$ and a shorter $\tau_{TADF}$ compared to the published TADF mononuclear CuI complexes and $Cu_4I_4$ nanoclusters,[9,11,25] implying stronger TADF characteristics.

Given that these inorganic−organic hybrid TADF nanoclusters have high photoluminescence QYs, low self-adsorption, and a good ability to harvest both singlet and triplet excitons, we were motivated to study their potential as scintillation materials. To assess their X-ray absorption capabilities, X-ray absorptions were calculated on the $\mathbf{Cu_2X_2}$ nanoclusters, and it was observed that the resonance absorption edges increased gradually from $\mathbf{Cu_2Cl_2}$ to $\mathbf{Cu_2I_2}$ because of the heavy atom effect (Figure S7). As shown in Figure S8, the RL spectrum showed negligible shifting compared to the PL spectrum at 300 K, indicating that the emission excited by ultraviolet (UV) and X-ray radiation likely originated from the same excited states. Respectively, the TADF $\mathbf{Cu_2Cl_2}$, $\mathbf{Cu_2Br_2}$, and $\mathbf{Cu_2I_2}$ nanoclusters exhibit RL responses that are 0.86-, 0.98-, and 2.01-fold higher than the scintillation standard (LYSO ∼ 33 200 photons $MeV^{-1}$)[41] with similar sample and reference thicknesses (Figure 1g and Table S4). It is important to note that the surfaces of the single-crystal reference samples were optically polished and that the $Cu_2X_2$ cluster samples contained microscale crystals with extremely smooth surfaces. Figure 1h shows a comparison of the X-ray attenuation efficiencies (XAEs) of the common inorganic X-ray scintillators BGO and LYSO, organic scintillator (DMAC-TRZ),[13] $Cu_4I_4$, and the $\mathbf{Cu_2X_2}$ nanoclusters. The TADF $\mathbf{Cu_2X_2}$ nanoclusters have relatively high XAEs, being 1 order of magnitude higher than those of organic TADF scintillating materials (Figure 1h). The $\mathbf{Cu_2I_2}$ nanocluster film with a thickness of 0.5 mm absorbs 38% X-ray radiation; in comparison, one of the best organic scintillators DMAC-TRZ can only achieve such a high XAE with a thickness of 6 mm.[13] Consequently, the light yields of $\mathbf{Cu_2Cl_2}$, $\mathbf{Cu_2Br_2}$, and $\mathbf{Cu_2I_2}$ were estimated to be 98 000 ± 4100, 102 400 ± 16 100, and 175 300 ± 4400 photons $MeV^{-1}$, respectively (Figures 1g and S10 and Table S4). The method for determining the light yield is given in the Supporting Information. To further ascertain the accuracy of the light yield measurements, we compared the nanoclusters to another common scintillator, BGO, and the published nanocluster scintillator $Cu_4I_4$[25] under identical experimental conditions (Figures 1g and S10 and Table S4). Both standards yielded light yield values for the $\mathbf{Cu_2X_2}$ nanoclusters that were in good agreement (Figure S10). Moreover, the relative light yields of $\mathbf{Cu_2I_2}$ and $\mathbf{Cu_2Br_2}$ were much higher than those of the reported phosphorescent tetranuclear Cu(I) iodide nanoclusters ($Cu_4I_4py_4$ and $Cu_4I_4(DBA)_4$)[11,25] and mononuclear Cu(I) halide complexes $[CuI(PPh_3)_2L]$[9] (Table S5). These results indicate that the synergistic effect of high X-ray absorption by heavy halogen atoms (Br or I) and the harvesting of both singlet and triplet excitons through TADF behaviors leads to enhanced light yields.

To gain insight into the electronic properties and the underlying luminescence mechanism of the TADF $\mathbf{Cu_2X_2}$ nanoclusters, we performed absorption spectral analysis and density functional theory (DFT) calculations. As shown in Figure S11, the absorption bands of all of the $\mathbf{Cu_2X_2}$ nanoclusters are presented with extinction coefficient values and suggestions for the corresponding transitions. The electronic absorption spectra of the $\mathbf{Cu_2X_2}$ nanoclusters display multiple absorption peaks in the range of 250−320 nm, which are assigned to ligand-centered (LC) $\pi-\pi^*$ transitions.[9,42,43] In


https://doi.org/10.1021/acsenergylett.3c02050
ACS Energy Lett. 2023, 8, 5088−5097

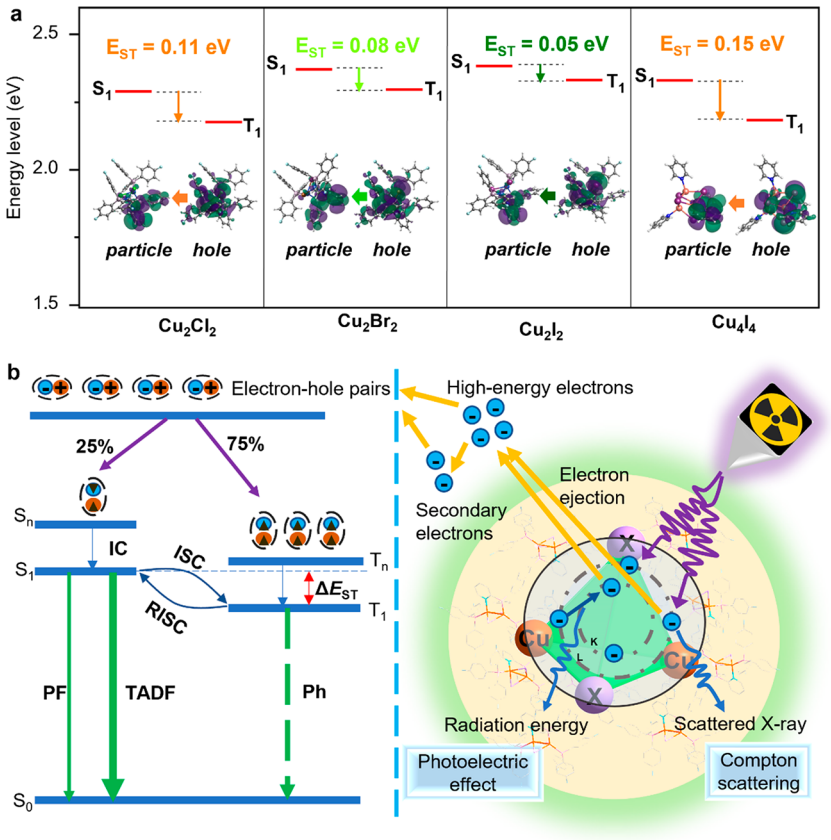


**Figure 2. DFT calculations and proposed mechanism of luminescence. (a) Calculated energy levels of the lowest singlet ($S_1$) and triplet ($T_1$) states for the $Cu_2X_2$ and $Cu_4I_4$ nanoclusters. Insets show the charge densities for the holes and particles from neutral orbital transitions from the ground state ($S_0$) to $S_1$. The DFT calculations were performed at the B3LYP/6-31G(d,p) + LANL2DZ level. (b) Proposed RL mechanism for the TADF $Cu_2X_2$ nanoclusters.**

addition, the low-energy absorption tails in the range of 330−410 nm are assigned to (metal and halogen)-to-ligand charge transfer (M+X)LCT transitions.[9,42,43] According to the theoretical absorption spectra of the $Cu_2X_2$ nanoclusters, the excited states with relatively high oscillator strength originate mainly from transitions from degenerate occupied orbitals (HOMO − 4 to HOMO (highest occupied molecular orbital)) to unoccupied orbitals ((lowest unoccupied molecular orbital) LUMO to LUMO + 1) (Figure S12 and Table S6). On the basis of the optimized geometries of $S_1$ and $T_1$ for the $Cu_2X_2$ and $Cu_4I_4$ nanoclusters, we conducted natural transition orbitals (NTOs) analysis, as shown in Figure 2a. For all three of the $Cu_2X_2$ nanoclusters, the optical absorption from the ground state ($S_0$) to $S_1$ can be attributed to the electronic transitions from the "hole" state delocalized in the $[Cu_2X_2]$ core to the "particle" state localized mainly within the bridging organic ligand Dppy. This suggests that the optical transition is characterized by a (M+X)LCT character between the $[Cu_2X_2]$ core and the bridging Dppy ligands, with negligible contribution from the monodentate P-donors. Structurally, the Cu−Cu interaction in $Cu_2I_2$ is larger than the intermolecular interactions of $Cu_2Cl_2$ and $Cu_2Br_2$ (Figure S1), which have been suggested to induce important or even unique photophysical/photochemical properties.[44] A stronger Cu−Cu interaction increases the possibility of orbital overlap, which affects luminescence performance.[44] This implies that $Cu_2I_2$ might emerge as one of the best TADF materials due to its potential balance between luminescence and orbital overlap. The DFT findings also point to a notable shift in the $Cu_2X_2$ series (Figure 2a and Table S2), with shifts approximating the $\Delta E(S_1-T_1)$ that is responsible for thermally activating TADF emission. The value of the RISC rate ($k_{RISC}$) is inversely correlated with $\Delta E_{ST}$ and positively correlated with the intensity of the SOC between singlet- and triplet-state orbits.[45] Therefore, decreasing $\Delta E_{ST}$ and increasing SOC are both beneficial for increasing $k_{RISC}$. In addition, the heavy atom effect mainly contributes to an increase in the SOC, resulting in a decrease in $\Delta E_{ST}$. Therefore, this effect results in a higher radiative TADF decay rate, allowing the emission QY to reach 86% for $Cu_2I_2$ at ambient temperature. Also, the emission maximum sequence (580 ($Cu_2Cl_2$), 550 ($Cu_2Br_2$), and 533 nm ($Cu_2I_2$)) corresponds to the order of the halide ligand field strengths ($I^- < Br^- < Cl^-$), leading to stronger d-orbital splitting and HOMO destabilization, thus ultimately reducing the energy gap. The results reveal a gradual decrease in the potential energy level difference due to the introduction of Br and I, significantly enhancing the orbital coupling between the singlet and triplet states. According to the above results, $Cu_2I_2$ has the strongest TADF character among the $Cu_2X_2$ complexes (Table S2). Figures S13 and S14 shows the calculated spin−orbit coupling matrix element (SOCME) values and oscillator strengths in the optimized $S_1$ of the $Cu_2I_2$ and $Cu_4I_4$ nanoclusters. Compared to the well-known cubane-like $Cu_4I_4$ nanoclusters, $Cu_2I_2$ shows a smaller $\Delta E_{ST}$ and a higher SOC between the singlet- and triplet-state orbits, which are both beneficial for increasing $k_{RISC}$ and greatly improving the ability to convert ionizing radiation into low-energy photons.[45,46]



https://doi.org/10.1021/acsenergylett.3c02050
ACS Energy Lett. 2023, 8, 5088−5097

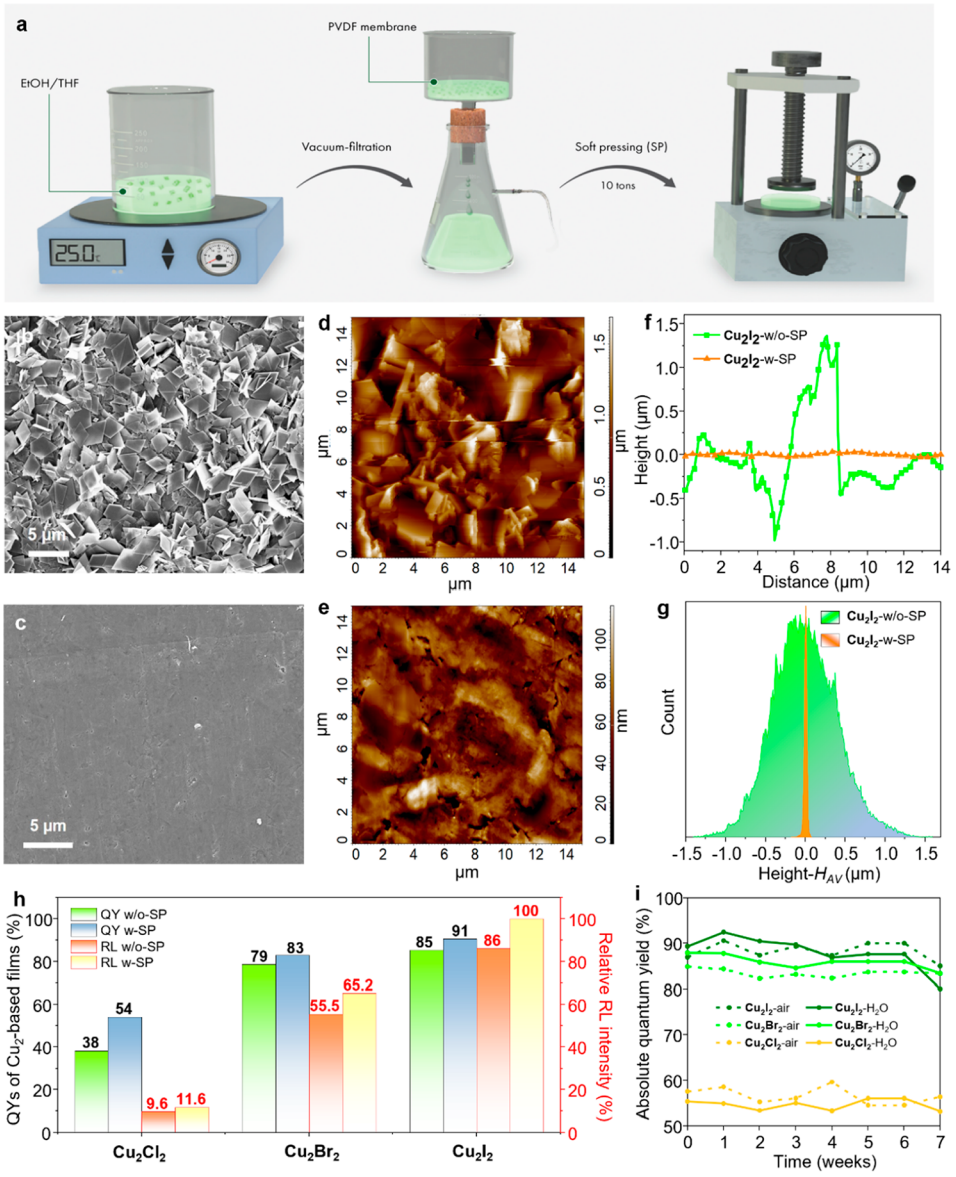


**Figure 3. Characterization of the $Cu_2X_2$ films. (a) Scheme of the $Cu_2X_2$ film synthesis procedure by suction filtration (w/o-SP) and soft-pressing (w-SP). SEM images of the front view of (b) $Cu_2I_2$-w/o-SP and (c) $Cu_2I_2$-w-SP. AFM images of (d) $Cu_2I_2$-w/o-SP and (e) $Cu_2I_2$-w-SP. (f) AFM line segment and (g) AFM height distribution analyses. (h) Comparison of QY and RL intensities of the $Cu_2X_2$ films (the integrated RL intensity of $Cu_2I_2$-w-SP was normalized to 100%). (i) The stability of these $Cu_2X_2$-w-SP films in an ambient atmosphere and in water.**

To understand the nature of the excited state of luminescent materials under high-energy X-ray radiation and low-energy photoexcitation, the PL and RL spectra of **$Cu_2X_2$** were compared at $T$ = 300 K (Figure S8). The agreement of both spectra indicates that, whether excited by UV or X-ray photons, the emission likely originates from the same excited states. Figure 2b schematically illustrates the proposed luminescence mechanism under X-ray irradiation for the **$Cu_2X_2$** nanoclusters. During the process of X-ray absorption and conversion, X-rays primarily interact with the heavy [$Cu_2X_2$] cores (Cu and X, especially Br and I) through the photoelectric effect and Compton scattering mechanism, resulting in the release of energetic electrons.[13,47] After being generated by electron−electron scattering and Auger processes, these hot electrons undergo rapid thermalization and are subsequently captured by the organic ligands within the **$Cu_2X_2$** nanocluster scintillators. Such interactions result in the creation of hole−electron pairs and a subsequent cascade of secondary electrons that exhibit characteristic (M+X)LCT and LCT states.[9,42] Thereafter, ∼25% of singlet excitons and ∼75% of triplet excitons are produced by charge recombination between the electrons and holes.[15,21] Finally, given the minimal $\Delta E_{ST}$ between $S_1$ and $T_1$ of the **$Cu_2X_2$** nanoclusters, the triplet excitons can efficiently transfer to singlet excitons via a RISC process. This results in efficient (M+X)LCT and LCT states for radiative processes, boasting higher internal quantum efficiencies and light yields. The highly radiative (M+X)LCT and LCT states, combined with the excellent RISC process, play a crucial role in enhancing the RL in the **$Cu_2X_2$** nanoclusters, thereby making them promising candidates for X-ray imaging.[42]



https://doi.org/10.1021/acsenergylett.3c02050
ACS Energy Lett. 2023, 8, 5088−5097

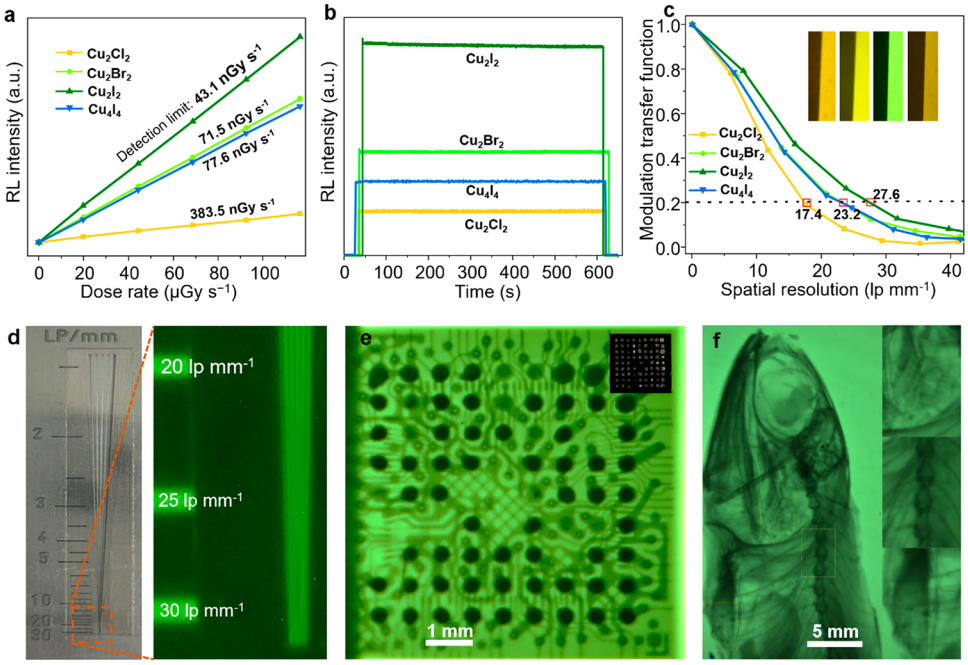


**Figure 4. X-ray imaging with the copper halide nanoclusters. (a) Detection limits of the $Cu_2$-based TADF films and the $Cu_4I_4$ film. (b) Normalized RL intensity at the corresponding emission maxima of the $Cu_2X_2$-w-SP TADF films and $Cu_4I_4$ film under continuous X-ray irradiation (dose rate of 146.5 $\mu$Gy $s^{-1}$). (c) Modulation transfer function (MTF) curves of the $Cu_2X_2$-w-SP TADF films and $Cu_4I_4$ film measured by the slanted-edge method (inset: corresponding X-ray edge images of the $Cu_2X_2$-w-SP TADF films). Bright-field and X-ray images using the $Cu_2I_2$-w-SP TADF film of (d) a standard line-pair card, (e) an electronic chip, and (f) a small fish (dose rate of 130 $\mu$Gy/s; exposure of 10 s).**

In recent years, there has been a growing interest in using environmentally friendly Cu-based materials with high luminescence efficiencies as scintillators.[7,9,11,25,41,48] The properties of these materials, however, are highly dependent on their manufacturing strategy. The most widely used strategies include polymer-based flexible films,[9,25,26,42] high-temperature transparent ceramics,[32,49] and high-pressure wafers.[11,33] Despite their promising properties, most CuI-based compounds exhibit strong mechanochromic luminescence[30,31] and aggregation-induced luminescence,[50,51] making it challenging to optimize the luminescence efficiency with respect to thickness and size using current preparation strategies. Fortunately, the recent development of a vacuum filtration strategy has provided a pathway to address these problems and has yielded excellent results for the application of nanoscale materials.[6,52]

A vacuum filtration strategy was successfully applied to the TADF $Cu_2X_2$ nanoclusters for the preparation of high-quality scintillator screens (Figure 3a). Because of their excellent solubility in tetrahydrofuran (THF), uniform rhomboidal microcrystals were first achieved by using ethanol as an antisolvent (the reaction is shown in the Supporting Information). The microcrystals, which had a relatively uniform size of about 2 $\mu$m, were analyzed by transmission electron microscopy (TEM) (Figures S15−S17) to confirm the elemental distributions. The obtained $Cu_2X_2$ microcrystals were then uniformly dispersed in a mixed solvent of THF and ethanol for the fabrication of stable and flexible screens. For vacuum filtration, a hydrophilic poly(vinylidene fluoride) (PVDF) filter membrane (Figure S18) was used to trap and support the hydrophobic $Cu_2X_2$ microcrystals. Scanning electron microscopy (SEM) was used to characterize the surface of the $Cu_2X_2$ films fabricated by vacuum filtration (abbreviated as $Cu_2X_2$-w/o-SP). The thicknesses of the $Cu_2X_2$ microcrystal layer and the PVDF membrane layer after vacuum filtration were 50 and 80 $\mu$m, respectively (Figure S19a). As shown in Figure 3b, the disordered surface arrangement of the PVDF membrane resulted in an uneven surface with numerous defects between adjacent $Cu_2X_2$ microcrystals, which could negatively impact future applications. To address this issue, soft-pressing was subsequently employed to obtain uniform and smooth films of the $Cu_2X_2$ microcrystals at a positive pressure of 10 tons (Figure 3a). The $Cu_2X_2$-based films after being soft-pressed (abbreviated as $Cu_2X_2$-w-SP) had a compact structure and a relatively flat surface (Figures 3c, S20, and S21), and the thicknesses of the $Cu_2X_2$ microcrystal layer and the PVDF membrane layer were reduced to 20 and 60 $\mu$m, respectively (Figure S19b). The surface quality of the achieved films was further evaluated by using atomic force microscopy (AFM) (Figure 3d,e). The root-mean-square roughnesses of the $Cu_2X_2$-w/o-SP and $Cu_2X_2$-w-SP films were calculated to be 400 and 19 nm, respectively, for areas of 15 × 15 $\mu m^2$. The roughness of the $Cu_2X_2$-w-SP film was greatly reduced compared to that of the $Cu_2X_2$-w/o-SP film, as evidenced by both the AFM line segment and height distribution analyses (panels f and g of Figure 3, respectively). Clearly, soft-pressing using 10 tons of pressure was sufficient in eliminating pores in the thick film and rearranging the $Cu_2X_2$ microcrystals. The obtained $Cu_2X_2$-w-SP films exhibited excellent uniformity under both UV and X-ray radiation, and the thickness and flexibility could be controlled by the amount of $Cu_2X_2$ microcrystals in the films (Figure S22).

Furthermore, the pressure stability greatly affects the subsequent scintillator properties of the $Cu_2X_2$-based films. Unlike most Cu−I nanoclusters (especially $Cu_4I_4$), which have excellent mechanochromic properties due to their structural


https://doi.org/10.1021/acsenergylett.3c02050
ACS Energy Lett. 2023, 8, 5088−5097

variation (Figure S23),[38,53] the good pressure stability of $Cu_2X_2$ was confirmed by powder X-ray diffraction (PXRD) diagrams and emission spectra before and after soft-pressing (Figure S24). In addition, the intensity of the (002) peak was found to be significantly enhanced, especially for $Cu_2I_2$ (Figure S24c), indicating a preferred orientation after laminating. Moreover, all of the $Cu_2X_2$ complexes exhibited large Stokes shifts, almost negligible self-adsorption, and high photoluminescence quantum yields (PLQYs) at room temperature (54% for $Cu_2Cl_2$-w-SP, 83% for $Cu_2Br_2$-w-SP, and 91% for $Cu_2I_2$-w-SP). The decrease in the amount of voids and pinholes in the soft-pressed $Cu_2X_2$-based films resulted in a remarkable enhancement in film quality, as evidenced by the increasing intensity of PL and RL, as shown in Figures 3h and S25. The substantial reduction in the porosity of the films effectively hinders ion migration, minimizes light-induced carrier trapping and recombination, and consequently leads to a reduction in X-ray scattering. Additionally, the $Cu_2X_2$-w-SP films showed excellent stability in both ambient atmosphere and water, surpassing traditional bulk X-ray scintillating and metal halide perovskites[47,53] (Figures 3i, S26, and S27).

To verify the scintillator properties of the $Cu_2X_2$-w-SP screens, linear responses were first obtained at higher dose rates ranging from 19.8 to 116.4 $\mu$Gy $s^{-1}$ (Figure S28), making them an excellent choice for achieving a good X-ray imaging contrast. The limit of detection (LOD) was determined based on a signal-to-noise ratio (SNR) of 3. In terms of response sensitivity, the inclusion of heavy elements (I and Br) significantly enhanced the response sensitivity of the scintillators to X-ray dose rates, with $Cu_2I_2$-w-SP exhibiting a response sensitivity of 43.1 nGy $s^{-1}$, as opposed to those of 383.5 and 71.5 nGy $s^{-1}$ for $Cu_2Cl_2$-w-SP and $Cu_2Br_2$-w-SP (almost the same as those of $Cu_4I_4$), respectively (Figure 4a). Remarkably, the X-ray dose rate of $Cu_2I_2$-w-SP was approximately 100 times lower than the requirement for standard diagnostic imaging (5.5 $\mu$Gy $s^{-1}$). Additionally, all of the $Cu_2X_2$-w-SP screens exhibited excellent RL stability, with the RL intensity remaining above 90% even when exposed to ionizing radiation at a dose rate of 146.5 $\mu$Gy $s^{-1}$ for a continuous duration of 600 s (Figure 4b).

Motivated by the promising luminescence properties of the TADF $Cu_2X_2$-w-SP screens, we investigated their imaging resolutions. The imaging resolutions followed the trend of RL intensity, with high resolutions being achieved for the $Cu_2X_2$-w-SP screen (Figures 4d and S29), according to a standard line-pair card. By calculating the modulation transfer function (MTF) of the standard X-ray slant image, we determined the spatial resolutions (at an MTF of 0.2; see Figures 4c and S30–S32) to be 17.4, 23.2, and 27.6 lp $mm^{-1}$ for $Cu_2Cl_2$, $Cu_2Br_2$, and $Cu_2I_2$, respectively. The high spatial imaging resolution of the TADF $Cu_2I_2$-w-SP screen surpasses that of most reported organic and inorganic materials, e.g., the $Cu_4I_4$ nanocluster (~23 lp $mm^{-1}$), further underscoring the promising practical potential of incorporating TADF chromophores into high-performance X-ray imaging scintillators using pressing engineering strategies. To demonstrate the practical value of the TADF scintillators, we conducted a series of imaging experiments. In particular, we employed the principle of X-ray contrast imaging to inspect the complex internal structures of two electronic chips of different sizes (Figures 4e, S33, and S34), which were opaque to visible light. The $Cu_2X_2$-w-SP scintillator screens enabled a clear visualization of the complex structure of the electronic chip. Figures 4e and S33 display the X-ray imaging of a targeted chip positioned on the complex $Cu_2I_2$-w-SP scintillator screen. Owing to the differential absorption of X-rays by different materials in the chip, the internal structure and circuitry beneath the black plate are clearly visible. A small sample of fish was also used to evaluate the potential of the $Cu_2X_2$-w-SP scintillator screens for biological applications (Figure 4f). As shown in Figures 4f and S34, the skeleton, head, and fin of the fish are clearly observable under X-ray exposure. We believe that such high resolution and superior imaging capability of the $Cu_2I_2$-w-SP TADF scintillator screen exceed those reported for most scintillators.[8−10,12,13,25,49,54,55] These results further demonstrate the promising potential of organic−inorganic hybrid TADF scintillators in medical diagnosis and industrial inspection.

In this study, we demonstrated a series of TADF $Cu_2X_2$ nanoclusters, which exhibit intense radioluminescence, low self-absorption, and high radiation stability. The efficient $[Cu_2X_2]$-to-ligand charge transfer characteristics of the nanoclusters contribute to their scintillation performance, which is superior to that of other copper halide nanoclusters, resulting in record-high relative light yields (as high as 175 000 photons $MeV^{-1}$ for $Cu_2I_2$). Because of their non-mechanochromic properties, flexible $Cu_2X_2$ TADF scintillation screens were successfully created through a soft-pressing strategy. These fabricated screens showcased an outstanding performance, having a detection limit as low as 43.1 nGy $s^{-1}$, an X-ray imaging resolution as high as 27.6 lp $mm^{-1}$, and a highly linear response to the X-ray dose rate. These findings highlight the potential of inorganic−organic hybrid metal nanoclusters in advancing the development of high-energy radiation scintillation materials.

## ■ ASSOCIATED CONTENT

### Supporting Information

The Supporting Information is available free of charge at https://pubs.acs.org/doi/10.1021/acsenergylett.3c02050.

Experimental section (material synthesis, material characterization descriptions, time-dependent DFT calculations, and light yield, XAE, and X-ray imaging spatial resolution calculations), temperature-dependent emission intensities, temperature-dependent decay time measurements, absorption spectra calculations, TEM and SEM images of crystals and scintillating films, EDS mapping of crystals, XRD analysis, quantum yield determination, X-ray images of objects, comparisons of light yields, comparison of X-ray detection and imaging with TADF scintillators, crystal data for the $Cu_2X_2$ nanoclusters, and details of literature comparisons (PDF)

## ■ AUTHOR INFORMATION

### Corresponding Authors

**Mehmet Bayindir** − *Center for Hybrid Nanostructures, University of Hamburg, Hamburg 22761, Germany;* orcid.org/0000-0003-0233-6870; Email: mehmet.bayindir@uni-hamburg.de

**Omar F. Mohammed** − *Advanced Membranes and Porous Materials Center, Division of Physical Science and Engineering, King Abdullah University of Science and Technology (KAUST), Thuwal 23955-6900, Saudi Arabia;*

orcid.org/0000-0001-8500-1130;
Email: omar.abdelsaboor@kaust.edu.sa

**Osman M. Bakr** − *KAUST Catalysis Center (KCC), Division of Physical Science and Engineering, King Abdullah University of Science and Technology (KAUST), Thuwal 23955-6900, Saudi Arabia;* orcid.org/0000-0002-3428-1002; Email: osman.bakr@kaust.edu.sa

## Authors

**Peng Yuan** − *KAUST Catalysis Center (KCC), Division of Physical Science and Engineering, King Abdullah University of Science and Technology (KAUST), Thuwal 23955-6900, Saudi Arabia*

**Tengyue He** − *Advanced Membranes and Porous Materials Center, Division of Physical Science and Engineering, King Abdullah University of Science and Technology (KAUST), Thuwal 23955-6900, Saudi Arabia*

**Yang Zhou** − *Advanced Membranes and Porous Materials Center, Division of Physical Science and Engineering, King Abdullah University of Science and Technology (KAUST), Thuwal 23955-6900, Saudi Arabia*

**Jun Yin** − *Department of Applied Physics, The Hong Kong Polytechnic University, Hong Kong 999077, China;* orcid.org/0000-0002-1749-1120

**Hansong Zhang** − *State Key Laboratory for Physical Chemistry of Solid Surfaces, Collaborative Innovation Center of Chemistry for Energy Materials, National & Local Joint Engineering Research Center of Preparation Technology of Nanomaterials, College of Chemistry and Chemical Engineering Xiamen University, Xiamen 361005, China*

**Yongcao Zhang** − *Division of Physical Science and Engineering, King Abdullah University of Science and Technology (KAUST), Thuwal 23955-6900, Saudi Arabia*

**Xiting Yuan** − *Advanced Membranes and Porous Materials Center, Division of Physical Science and Engineering, King Abdullah University of Science and Technology (KAUST), Thuwal 23955-6900, Saudi Arabia*

**Chunwei Dong** − *KAUST Catalysis Center (KCC), Division of Physical Science and Engineering, King Abdullah University of Science and Technology (KAUST), Thuwal 23955-6900, Saudi Arabia;* orcid.org/0000-0002-5788-8819

**Renwu Huang** − *KAUST Catalysis Center (KCC), Division of Physical Science and Engineering, King Abdullah University of Science and Technology (KAUST), Thuwal 23955-6900, Saudi Arabia*

**Wenyi Shao** − *Advanced Membranes and Porous Materials Center, Division of Physical Science and Engineering, King Abdullah University of Science and Technology (KAUST), Thuwal 23955-6900, Saudi Arabia;* orcid.org/0000-0003-2761-7310

**Shulin Chen** − *KAUST Catalysis Center (KCC), Division of Physical Science and Engineering, King Abdullah University of Science and Technology (KAUST), Thuwal 23955-6900, Saudi Arabia*

**Xin Song** − *KAUST Catalysis Center (KCC), Division of Physical Science and Engineering, King Abdullah University of Science and Technology (KAUST), Thuwal 23955-6900, Saudi Arabia;* orcid.org/0000-0003-3342-9455

**Renqian Zhou** − *KAUST Catalysis Center (KCC), Division of Physical Science and Engineering, King Abdullah University of Science and Technology (KAUST), Thuwal 23955-6900, Saudi Arabia*

**Nanfeng Zheng** − *State Key Laboratory for Physical Chemistry of Solid Surfaces, Collaborative Innovation Center of Chemistry for Energy Materials, National & Local Joint Engineering Research Center of Preparation Technology of Nanomaterials, College of Chemistry and Chemical Engineering Xiamen University, Xiamen 361005, China;* orcid.org/0000-0001-9879-4790

**Mutalifu Abulikemu** − *KAUST Catalysis Center (KCC), Division of Physical Science and Engineering, King Abdullah University of Science and Technology (KAUST), Thuwal 23955-6900, Saudi Arabia*

**Mohamed Eddaoudi** − *Advanced Membranes and Porous Materials Center, Division of Physical Science and Engineering, King Abdullah University of Science and Technology (KAUST), Thuwal 23955-6900, Saudi Arabia;* orcid.org/0000-0003-1916-9837

Complete contact information is available at: https://pubs.acs.org/10.1021/acsenergylett.3c02050

## Author Contributions

[+]P.Y., T.H., Y.Z., and J.Y. contributed equally to this work.

## Notes

The authors declare the following competing financial interest(s): O.M.B. is a founder of Quantum Solutions, a company that develops optoelectronic devices.

## ■ ACKNOWLEDGMENTS

This work was supported by King Abdullah University of Science and Technology (KAUST), the National Key R&D Program of China (2017YFA0207302), the National Natural Science Foundation of China (21890752, 21731005, and 21721001) and the 111 Project (B08027). M.B. thanks the Alexander von Humboldt Foundation for the financial support.

## ■ REFERENCES

(1) Ou, X.; Qin, X.; Huang, B.; Zan, J.; Wu, Q.; Hong, Z.; Xie, L.; Bian, H.; Yi, Z.; Chen, X.; Wu, Y.; Song, X.; Li, J.; Chen, Q.; Yang, H.; Liu, X. High-Resolution X-ray Luminescence Extension Imaging. *Nature* **2021**, *590* (7846), 410−415.

(2) Chen, Q.; Wu, J.; Ou, X.; Huang, B.; Almutlaq, J.; Zhumekenov, A. A.; Guan, X.; Han, S.; Liang, L.; Yi, Z.; Li, J.; Xie, X.; Wang, Y.; Li, Y.; Fan, D.; Teh, D. B. L.; All, A. H.; Mohammed, O. F.; Bakr, O. M.; Wu, T.; Bettinelli, M.; Yang, H.; Huang, W.; Liu, X. All-Inorganic Perovskite Nanocrystal Scintillators. *Nature* **2018**, *561* (7721), 88−93.

(3) Cao, F.; Yu, D.; Ma, W.; Xu, X.; Cai, B.; Yang, Y. M.; Liu, S.; He, L.; Ke, Y.; Lan, S.; Choy, K. L.; Zeng, H. Shining Emitter in a Stable Host: Design of Halide Perovskite Scintillators for X-ray Imaging from Commercial Concept. *ACS Nano* **2020**, *14* (5), 5183−5193.

(4) Wu, Y.; Feng, J.; Yang, Z.; Liu, Y.; Liu, S. Halide Perovskite: A Promising Candidate for Next-Generation X-Ray Detectors. *Adv. Sci.* **2023**, *10* (1), No. 2205536.

(5) Li, X.; Hu, X.; Li, C.; Yang, W.; Wang, C.; Chen, Y.; Zeng, H. Are Inorganic Lead Halide Perovskite Nanocrystals Promising Scintillators? *ACS Energy Lett.* **2023**, *8* (7), 2996−3004.

(6) Huang, R. W.; Song, X.; Chen, S.; Yin, J.; Maity, P.; Wang, J.; Shao, B.; Zhu, H.; Dong, C.; Yuan, P.; Ahmad, T.; Mohammed, O. F.; Bakr, O. M. Radioluminescent Cu-Au Metal Nanoclusters: Synthesis and Self-Assembly for Efficient X-ray Scintillation and Imaging. *J. Am. Chem. Soc.* **2023**, *145* (25), 13816−13827.

(7) Zhou, Y.; Wang, X.; He, T.; Yang, H.; Yang, C.; Shao, B.; Gutiérrez-Arzaluz, L.; Bakr, O. M.; Zhang, Y.; Mohammed, O. F. Large-Area Perovskite-Related Copper Halide Film for High-Resolution Flexible X-ray Imaging Scintillation Screens. *ACS Energy Lett.* **2022**, *7* (2), 844−846.

(8) Han, K.; Sakhatskyi, K.; Jin, J.; Zhang, Q.; Kovalenko, M. V.; Xia, Z. Seed-Crystal-Induced Cold Sintering Toward Metal Halide Transparent Ceramic Scintillators. *Adv. Mater.* **2022**, *34* (17), No. 2110420.
(9) Liu, X.; Jiang, Y.; Li, F.; Xu, X.; Li, R.; Zhu, W.; Ni, J.; Ding, C.; Liu, S.; Zhao, Q. Thermally Activated Delayed Fluorescent Scintillators Based on Mononuclear Copper(I) Halide Complexes for High-Resolution X-Ray Imaging. *Adv. Opt. Mater.* **2023**, *11* (4), No. 2202169.
(10) Zhang, F.; Zhou, Y.; Chen, Z.; Wang, M.; Ma, Z.; Chen, X.; Jia, M.; Wu, D.; Xiao, J.; Li, X.; Zhang, Y.; Shi, Z.; Shan, C. Thermally Activated Delayed Fluorescence Zirconium-Based Perovskites for Large-Area and Ultraflexible X-ray Scintillator Screens. *Adv. Mater.* **2022**, *34* (43), No. 2270301.
(11) Hu, Q.; Zhang, C.; Wu, X.; Liang, G.; Wang, L.; Niu, X.; Wang, Z.; Si, W.-D.; Han, Y.; Huang, R.; Xiao, J.; Sun, D. Highly Effective Hybrid Copper(I) Iodide Cluster Emitter with Negative Thermal Quenched Phosphorescence for X-Ray Imaging. *Angew. Chem., Int. Ed.* **2023**, *62* (11), No. e202217784.
(12) Wang, J.-X.; Gutiérrez-Arzaluz, L.; Wang, X.; He, T.; Zhang, Y.; Eddaoudi, M.; Bakr, O. M.; Mohammed, O. F. Heavy-Atom Engineering of Thermally Activated Delayed Fluorophores for High-Performance X-ray Imaging Scintillators. *Nat. Photonics* **2022**, *16* (12), 869−875.
(13) Ma, W.; Su, Y.; Zhang, Q.; Deng, C.; Pasquali, L.; Zhu, W.; Tian, Y.; Ran, P.; Chen, Z.; Yang, G.; Liang, G.; Liu, T.; Zhu, H.; Huang, P.; Zhong, H.; Wang, K.; Peng, S.; Xia, J.; Liu, H.; Liu, X.; Yang, Y. M. Thermally Activated Delayed Fluorescence (TADF) Organic Molecules for Efficient X-ray Scintillation and Imaging. *Nat. Mater.* **2022**, *21* (2), 210−216.
(14) Peng, Q. C.; Si, Y. B.; Wang, Z. Y.; Dai, S. H.; Chen, Q. S.; Li, K.; Zang, S. Q. Thermally Activated Delayed Fluorescence Coinage Metal Cluster Scintillator. *ACS Cent. Sci.* **2023**, *9* (7), 1419−1426.
(15) Chen, X. K.; Kim, D.; Bredas, J. L. Thermally Activated Delayed Fluorescence (TADF) Path toward Efficient Electroluminescence in Purely Organic Materials: Molecular Level Insight. *Acc. Chem. Res.* **2018**, *51* (9), 2215−2224.
(16) Yang, Z.; Mao, Z.; Xie, Z.; Zhang, Y.; Liu, S.; Zhao, J.; Xu, J.; Chi, Z.; Aldred, M. P. Recent Advances in Organic Thermally Activated Delayed Fluorescence Materials. *Chem. Soc. Rev.* **2017**, *46* (3), 915−1016.
(17) Uoyama, H.; Goushi, K.; Shizu, K.; Nomura, H.; Adachi, C. Highly Efficient Organic Light-emitting Diodes from Delayed Fluorescence. *Nature* **2012**, *492* (7428), 234−8.
(18) Yersin, H.; Czerwieniec, R.; Shafikov, M. Z.; Suleymanova, A. F. TADF Material Design: Photophysical Background and Case Studies Focusing on Cu(I) and Ag(I) Complexes. *ChemPhysChem* **2017**, *18* (24), 3508−3535.
(19) Hofbeck, T.; Monkowius, U.; Yersin, H. Highly Efficient Luminescence of Cu(I) Compounds: Thermally Activated Delayed Fluorescence Combined with Short-Lived Phosphorescence. *J. Am. Chem. Soc.* **2015**, *137* (1), 399−404.
(20) Tao, Y.; Yuan, K.; Chen, T.; Xu, P.; Li, H.; Chen, R.; Zheng, C.; Zhang, L.; Huang, W. Thermally Activated Delayed Fluorescence Materials towards the Breakthrough of Organoelectronics. *Adv. Mater.* **2014**, *26* (47), 7931−7958.
(21) Han, Z.; Dong, X.-Y.; Zang, S.-Q. Crystalline Metal-Organic Materials with Thermally Activated Delayed Fluorescence. *Adv. Opt. Mater.* **2021**, *9* (23), No. 2100081.
(22) Tang, X.; Cui, L. S.; Li, H. C.; Gillett, A. J.; Auras, F.; Qu, Y. K.; Zhong, C.; Jones, S. T. E.; Jiang, Z. Q.; Friend, R. H.; Liao, L. S. Highly Efficient Luminescence from Space-Confined Charge-Transfer Emitters. *Nat. Mater.* **2020**, *19* (12), 1332−1338.
(23) Kaji, H.; Suzuki, H.; Fukushima, T.; Shizu, K.; Suzuki, K.; Kubo, S.; Komino, T.; Oiwa, H.; Suzuki, F.; Wakamiya, A.; Murata, Y.; Adachi, C. Purely Organic Electroluminescent Material Realizing 100% Conversion from Electricity to Light. *Nat. Commun.* **2015**, *6* (1), 8476.
(24) Sato, K.; Shizu, K.; Yoshimura, K.; Kawada, A.; Miyazaki, H.; Adachi, C. Organic Luminescent Molecule with Energetically Equivalent Singlet and Triplet Excited States for Organic Light-Emitting Diodes. *Phys. Rev. Lett.* **2013**, *110* (24), No. 247401.
(25) Zhao, W.; Wang, Y.; Guo, Y.; Suh, Y. D.; Liu, X. Color-Tunable and Stable Copper Iodide Cluster Scintillators for Efficient X-Ray Imaging. *Adv. Sci.* **2023**, *10* (5), No. 2205526.
(26) Han, K.; Jin, J.; Su, B.; Qiao, J.; Xia, Z. Promoting Single Channel Photon Emission in Copper(I) Halide Clusters for X-Ray Detection. *Adv. Opt. Mater.* **2022**, *10* (20), No. 2200865.
(27) Zhao, J.; Zhao, L.; Deng, Y.; Xiao, X.; Ni, Z.; Xu, S.; Huang, J. Perovskite-Filled Membranes for Flexible and Large-Area Direct-Conversion X-Ray Detector Arrays. *Nat. Photonics* **2020**, *14* (10), 612−617.
(28) Hong, Z.; Chen, Z.; Chen, Q.; Yang, H. Advancing X-ray Luminescence for Imaging, Biosensing, and Theragnostics. *Acc. Chem. Res.* **2023**, *56* (1), 37−51.
(29) Jia, B.; Chu, D.; Li, N.; Zhang, Y.; Yang, Z.; Hu, Y.; Zhao, Z.; Feng, J.; Ren, X.; Zhang, H.; Zhao, G.; Sun, H.; Yuan, N.; Ding, J.; Liu, Y.; Liu, S. F. Airflow-Controlled Crystallization for a Multi-Inch 2D Halide Perovskite Single-Crystal Scintillator for Fast High-Resolution X-ray Imaging. *ACS Energy Lett.* **2023**, *8* (1), 590−599.
(30) Benito, Q.; Le Goff, X. F.; Maron, S.; Fargues, A.; Garcia, A.; Martineau, C.; Taulelle, F.; Kahlal, S.; Gacoin, T.; Boilot, J. P.; Perruchas, S. Polymorphic Copper Iodide Clusters: Insights into the Mechanochromic Luminescence Properties. *J. Am. Chem. Soc.* **2014**, *136* (32), 11311−11320.
(31) Perruchas, S.; Le Goff, X. F.; Maron, S.; Maurin, I.; Guillen, F.; Garcia, A.; Gacoin, T.; Boilot, J. P. Mechanochromic and Thermochromic Luminescence of A Copper Iodide Cluster. *J. Am. Chem. Soc.* **2010**, *132* (32), 10967−10969.
(32) Li, N.; Li, Y.; Xie, S.; Wu, J.; Liu, N.; Yu, Y.; Lin, Q.; Liu, Y.; Yang, S.; Lian, G.; Fang, Y.; Yang, D.; Chen, Z.; Tao, X. High-Performance and Self-Powered X-Ray Detectors Made of Smooth Perovskite Microcrystalline Films with 100-mum Grains. *Angew. Chem., Int. Ed.* **2023**, *62* (19), No. e202302435.
(33) Xia, M.; Song, Z.; Wu, H.; Du, X.; He, X.; Pang, J.; Luo, H.; Jin, L.; Li, G.; Niu, G.; Tang, J. Compact and Large-Area Perovskite Films Achieved via Soft-Pressing and Multi-Functional Polymerizable Binder for Flat-Panel X-Ray Imager. *Adv. Funct. Mater.* **2022**, *32* (16), No. 2110729.
(34) Ji, T.; Wang, T.; Li, H.; Peng, Q.; Tang, H.; Hu, S.; Yakovlev, A.; Zhong, Y.; Xu, X. $Ce^{3+}$-Doped Yttrium Aluminum Garnet Transparent Ceramics for High-Resolution X-Ray Imaging. *Adv. Opt. Mater.* **2022**, *10* (6), No. 2102056.
(35) Busch, J. M.; Zink, D. M.; Di Martino-Fumo, P.; Rehak, F. R.; Boden, P.; Steiger, S.; Fuhr, O.; Nieger, M.; Klopper, W.; Gerhards, M.; Brase, S. Highly Soluble Fluorine Containing Cu(I) AlkylPyrPhos TADF Complexes. *Dalton Trans.* **2019**, *48* (41), 15687−15698.
(36) Hofbeck, T.; Niehaus, T. A.; Fleck, M.; Monkowius, U.; Yersin, H. P∩N Bridged Cu(I) Dimers Featuring Both TADF and Phosphorescence. From Overview towards Detailed Case Study of the Excited Singlet and Triplet States. *Molecules* **2021**, *26* (11), 3415.
(37) Czerwieniec, R.; Leitl, M. J.; Homeier, H. H. H.; Yersin, H. Cu(I) Complexes−Thermally Activated Delayed Fluorescence. Photophysical Approach and Material Design. *Coord. Chem. Rev.* **2016**, *325*, 2−28.
(38) Ford, P. C.; Cariati, E.; Bourassa, J. Photoluminescence Properties of Multinuclear Copper(I) Compounds. *Chem. Rev.* **1999**, *99* (12), 3625−3648.
(39) Liu, J.; Wang, N.; Yu, Y.; Yan, Y.; Zhang, H.; Li, J.; Yu, J. Carbon Dots in Zeolites: A New Class of Thermally Activated Delayed Fluorescence Materials with Ultralong Lifetimes. *Sci. Adv.* **2017**, *3* (5), No. e1603171.
(40) Leitl, M. J.; Krylova, V. A.; Djurovich, P. I.; Thompson, M. E.; Yersin, H. Phosphorescence versus Thermally Activated Delayed Fluorescence. Controlling Singlet-Triplet Splitting in Brightly Emitting and Sublimable Cu(I) Compounds. *J. Am. Chem. Soc.* **2014**, *136* (45), 16032−8.


https://doi.org/10.1021/acsenergylett.3c02050
*ACS Energy Lett.* 2023, 8, 5088−5097

(41) He, T.; Zhou, Y.; Yuan, P.; Yin, J.; Gutiérrez-Arzaluz, L.; Chen, S.; Wang, J.-X.; Thomas, S.; Alshareef, H. N.; Bakr, O. M.; Mohammed, O. F. Copper Iodide Inks for High-Resolution X-ray Imaging Screens. *ACS Energy Lett.* **2023**, *8*, 1362−1370.
(42) Zhang, N.; Qu, L.; Dai, S.; Xie, G.; Han, C.; Zhang, J.; Huo, R.; Hu, H.; Chen, Q.; Huang, W.; Xu, H. Intramolecular Charge Transfer Enables Highly-Efficient X-ray Luminescence in Cluster Scintillators. *Nat. Commun.* **2023**, *14* (1), 2901.
(43) Zink, D. M.; Bachle, M.; Baumann, T.; Nieger, M.; Kuhn, M.; Wang, C.; Klopper, W.; Monkowius, U.; Hofbeck, T.; Yersin, H.; Brase, S. Synthesis, Structure, and Characterization of Dinuclear Copper(I) Halide Complexes with P∧N Ligands Featuring Exciting Photoluminescence Properties. *Inorg. Chem.* **2013**, *52* (5), 2292−305.
(44) Gong, F.; Wang, Q.; Chen, J.; Yang, Z.; Liu, M.; Li, S.; Yang, G.; Bai, L.; Liu, J.; Dong, Y. Exploring Intertrimer Cu···Cu Interactions and Further Phosphorescent Properties of Aryl Trimer Copper(I) Pyrazolates via Substituent Changing and External Pressure. *Inorg. Chem.* **2010**, *49* (4), 1658−66.
(45) Hu, Y. X.; Miao, J.; Hua, T.; Huang, Z.; Qi, Y.; Zou, Y.; Qiu, Y.; Xia, H.; Liu, H.; Cao, X.; Yang, C. Efficient Selenium-Integrated TADF OLEDs with Reduced Roll-off. *Nat. Photonics* **2022**, *16* (11), 803−810.
(46) Ansari, R.; Shao, W.; Yoon, S. J.; Kim, J.; Kieffer, J. Charge Transfer as the Key Parameter Affecting the Color Purity of Thermally Activated Delayed Fluorescence Emitters. *ACS Appl. Mater. Interfaces* **2021**, *13* (24), 28529−28537.
(47) Zhou, Y.; Chen, J.; Bakr, O. M.; Mohammed, O. F. Metal Halide Perovskites for X-ray Imaging Scintillators and Detectors. *ACS Energy Lett.* **2021**, *6* (2), 739−768.
(48) Liu, X.; Li, R.; Xu, X.; Jiang, Y.; Zhu, W.; Yao, Y.; Li, F.; Tao, X.; Liu, S.; Huang, W.; Zhao, Q. Lanthanide(III)-$Cu_4I_4$ Organic Framework Scintillators Sensitized by Cluster-based Antenna for High-Resolution X-ray Imaging. *Adv. Mater.* **2023**, *35* (8), No. 2206741.
(49) Su, B.; Jin, J.; Han, K.; Xia, Z. Ceramic Wafer Scintillation Screen by Utilizing Near-Unity Blue-Emitting Lead-Free Metal Halide $(C_8H_{20}N)_2Cu_2Br_4$. *Adv. Funct. Mater.* **2023**, *33* (5), No. 2210735.
(50) Li, H.; Lv, Y.; Zhou, Z.; Tong, H.; Liu, W.; Ouyang, G. Coordinated Anionic Inorganic Module-An Efficient Approach Towards Highly Efficient Blue-Emitting Copper Halide Ionic Hybrid Structures. *Angew. Chem., Int. Ed.* **2022**, *61* (8), No. e202115225.
(51) Chen, C.; Li, R. H.; Zhu, B. S.; Wang, K. H.; Yao, J. S.; Yin, Y. C.; Yao, M. M.; Yao, H. B.; Yu, S. H. Highly Luminescent Inks: Aggregation-Induced Emission of Copper-Iodine Hybrid Clusters. *Angew. Chem., Int. Ed.* **2018**, *57* (24), 7106−7110.
(52) Wu, X.; Guo, Z.; Zhu, S.; Zhang, B.; Guo, S.; Dong, X.; Mei, L.; Liu, R.; Su, C.; Gu, Z. Ultrathin, Transparent, and High Density Perovskite Scintillator Film for High Resolution X-Ray Microscopic Imaging. *Adv. Sci.* **2022**, *9* (17), No. 2200831.
(53) Troyano, J.; Zamora, F.; Delgado, S. Copper(I)-Iodide Cluster Structures as Functional and Processable Platform Materials. *Chem. Soc. Rev.* **2021**, *50* (7), 4606−4628.
(54) Liu, Y.; Li, C.; Ren, Z.; Yan, S.; Bryce, M. R. All-Organic Thermally Activated Delayed Fluorescence Materials for Organic Light-Emitting Diodes. *Nat. Rev. Mater.* **2018**, *3* (4), 18020.
(55) Pan, W.; Yang, B.; Niu, G.; Xue, K.-H.; Du, X.; Yin, L.; Zhang, M.; Wu, H.; Miao, X.-S.; Tang, J. Hot-Pressed $CsPbBr_3$ Quasi-Monocrystalline Film for Sensitive Direct X-ray Detection. *Adv. Mater.* **2019**, *31* (44), No. 1904405.


https://doi.org/10.1021/acsenergylett.3c02050
*ACS Energy Lett.* 2023, 8, 5088−5097